



RESEARCH LETTER

10.1029/2022GL098666

Key Points:

- Measurement of three-dimensional surface displacement field produced by extensional dip-slip earthquake
- Application of optical image correlation to historical aerial imagery, thus expanding the window of remote geodetic observation
- Detection of previously unrecognized surface ruptures probably associated with the 1959 Hebgen Lake earthquake

Supporting Information:

Supporting Information may be found in the online version of this article.

Correspondence to:

L. Andreuttiova,
lucia.andreuttiova.16@ucl.ac.uk

Citation:

Andreuttiova, L., Hollingsworth, J., Vermeesch, P., Mitchell, T. M., & Bergman, E. (2022). Revisiting the 1959 Hebgen Lake earthquake using optical image correlation; new constraints on near-field 3D ground displacement. *Geophysical Research Letters*, 49, e2022GL098666. <https://doi.org/10.1029/2022GL098666>

Received 15 MAR 2022

Accepted 25 JUL 2022

© 2022. The Authors.

This is an open access article under the terms of the [Creative Commons Attribution License](#), which permits use, distribution and reproduction in any medium, provided the original work is properly cited.

Revisiting the 1959 Hebgen Lake Earthquake Using Optical Image Correlation; New Constraints on Near-Field 3D Ground Displacement

Lucia Andreuttiova¹ , James Hollingsworth² , Pieter Vermeesch¹ , Thomas M. Mitchell¹ , and Eric Bergman³

¹Department of Earth Sciences, University College London, London, UK, ²Université Grenoble Alpes, Université Savoie Mont Blanc, CNRS, IRD, Université Gustave Eiffel, Grenoble, France, ³Global Seismological Services, Golden, CO, USA

Abstract Near-field surface displacement measurements allow us to quantify the on- and off-fault proportion of earthquake-related deformation. The Hebgen Lake earthquake was a large normal event with a complex surface rupture, which broke across mountainous terrain. This study takes advantage of high-resolution historical aerial stereo-imagery to measure three-dimensional displacement from correlation of the orthorectified pre- and post-earthquake image mosaics. The results reveal new strike-slip ruptures which are possibly associated with the aftershocks from 18th August 1959. These structures likely reflect internal block deformation induced by the complex geometry of the mainshock. Additionally, comparison of our results with the existing displacement data shows that the optical image correlation-derived offsets often exceed the field measurements by >50%. We attribute this difference to inelastic off-fault deformation.

Plain Language Summary This study quantifies the surface deformation created by the 1959 Hebgen Lake earthquake. To measure the displacement field we use optical image correlation (OIC). OIC compares the pixel locations in the pre-earthquake and post-earthquake image and calculates any displacement from the pixel-shift. The images cover a large area, which enabled us to find new fault ruptures that slipped between 1947 and 1977. We also measured the displacement everywhere along the Red Canyon fault. Our displacement estimates are twice as large as those measured in the field. We think this is because our values capture diffuse displacement away from the main fault, whereas the field measurements only reveal the localized component of displacement on the fault plane. This study aims to improve understanding of how fault ruptures distribute slip into their surroundings, which in turn has important implications for how we assess their seismic hazard.

1. Introduction

The Hebgen Lake earthquake occurred on the 18th August (GMT) 1959 in SW Montana, U.S. This region lies within a zone of slow intracontinental extension, at the intersection between the Yellowstone volcanic system and the Intermountain Seismic Belt (Chang et al., 2013; Smith & Sbar, 1974). The Hebgen Lake earthquake was preceded by at least two events with similar magnitude that were dated at 1–3 and 10–14.5 ka by cosmogenic nuclide geochronology (Schwartz et al., 2009; Zreda & Noller, 1998). The 1959 event consisted of two sub-events with magnitude 7.0 and 6.3, separated by a 5-s time interval, and was followed by large aftershocks on the 18th and 19th of August (Doser, 1985). The subsidence associated with the Hebgen Lake earthquake was recorded over a broad area of approximately 1,500 km², and more than 150 km² subsided by more than 3.1 m (Myers & Hamilton, 1964).

The earthquake produced structurally complex surface ruptures with notable displacements along the Hebgen fault (HF), the Red Canyon fault (RCF), the Kirkwood fault (KF), and the West Fork fault (WFF). These are west-dipping normal faults with a cumulative length of approximately 35.4 km and maximum vertical offsets of 6.1, 5.8, 0.6, and 1.2 m, respectively (Figure 1, Witkind et al., 1962). Despite some geometric complexity, the ruptures generally strike $130^\circ \pm 10^\circ$, consistent with the fault plane solution from the main shock (Barrientos et al., 1989; Doser, 1985), and dip SW by 50° – 85° (Witkind, 1964). Doser (1985) and Ryall (1962) locate the epicenter 15 km northeast of Hebgen Lake, with a depth of approximately 15–25 km. However, uncertainty in the location, and especially the depth of the hypocenter makes it difficult to assess the spatial relationship between the source and the surface ruptures (Doser, 1985).

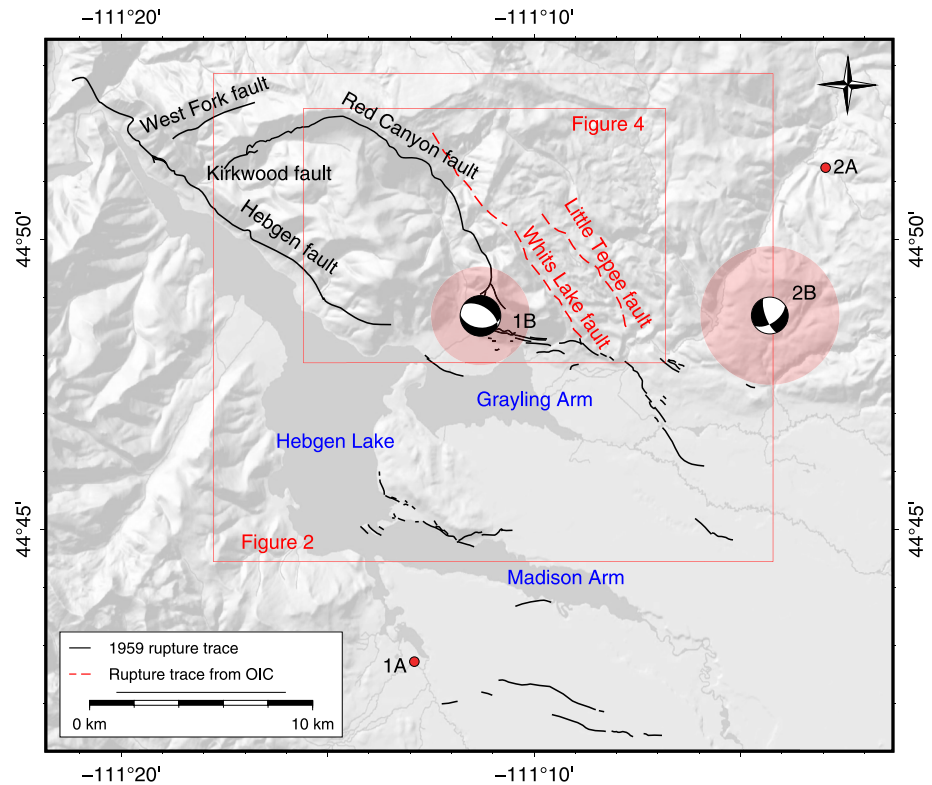


Figure 1. Overview of the earthquake area: the 1959 rupture trace mapped by the USGS (solid black line), previously unmapped faults, the Whits Lake fault and the Little Teepee fault (red dashed line), 1A and 2A are the initial locations of the main-shock and aftershock on 18 August 1959, respectively (from the USGS earthquake catalog), 1B and 2B are relocated earthquakes with their respective confidence ellipses determined in this study; focal mechanisms are from Doser (1985). The focal mechanism for 1B (strike = 95, dip = 42, rake = -111) is consistent with the NW-SE trending normal faulting while 2B (strike = 159, dip = 71, rake = -144) appears to correlate with the right-lateral movement on the Whits Lake fault. The red rectangles highlight areas of subsequent figures. The hillshaded DEM is ESRI Shaded Relief (resolution 10 m/px).

Previous studies measured the surface fault offset in the field (Witkind, 1964) and from an airborne LiDAR surface model (Johnson et al., 2018). The average offset measured in the field along the RCF and HF scarps was ~ 2.4 and ~ 1.6 m, respectively. When extrapolated over a 0–15 km depth range, and assuming a fault dip of 70° , the resulting seismic moments for each scarp, 2.9×10^{19} and 1.2×10^{19} Nm, are significantly lower than the seismologically derived moment release (Doser, 1985). This implies that either (a) slip on the fault plane at seismogenic depth is higher than the slip recorded at the surface (also known as shallow slip deficit (SSD), e.g., Fialko et al., 2005), or that (b) the large proportion of the earthquake-related inelastic deformation is distributed away from the fault-plane in the form of off-fault deformation (OFD) (e.g., C. W. Milliner et al., 2015). While dynamic rupture models suggest that some proportion of SSD may reflect the influence of the free surface on the updip propagation of slip on normal faults (Oglesby et al., 2000), relatively few examples of such a marked SSD have been observed on large magnitude ($M_w 7+$) surface rupturing normal earthquakes. This is due to their relative paucity compared with strike-slip and thrust events (Neely & Stein, 2021). Nevertheless, for a range of smaller normal events, SSD has also been observed (G. Xu et al., 2019). This contrasts with surface rupturing thrust events, for example, 1972 San Fernando (Heaton, 1982), or 1999 Chi Chi (Dominguez et al., 2003) earthquake, which featured larger slip at the surface than at depth. Several examples of SSD have also been reported for surface rupturing strike-slip faults (e.g., Jin & Fialko, 2021), based on inversion of satellite geodetic data. However, simplifications in the forward model, and the sampling of the geodetic data prior to inversion can both significantly overestimate the SSD (e.g., Magen et al., 2020; Marchandon et al., 2021; X. Xu et al., 2016). Distributed OFD is also thought to play a significant role in accommodating co-seismic slip (Mitchell & Faulkner, 2009) and can be observed over a range of spatial scales (from mm, Ostermeijer et al. (2020) to km, X. Xu et al. (2020)). Therefore, estimates of SSD based on simple elastic inversion of geodetic data, which do not account for OFD, may be biased too high in some cases (Marchandon et al., 2021; Scott et al., 2018).

In this study we use optical image correlation (OIC) of historical aerial photographs to better quantify the near-field surface displacement produced during the 1959 Hebgen Lake earthquake. We take advantage of the stereo-overlap between aerial photos to resolve the vertical displacement, which is the dominant displacement component in the Hebgen Lake earthquake. This approach is especially valuable for the pre-InSAR time-period (pre 1992), for which there are no other methods for creating dense maps of ground displacement. Furthermore, while recent studies have highlighted a link between OFD and fault zone maturity (Dolan & Haravitch, 2014), rupture kinematics (C. Milliner et al., 2021), and dynamics (Jara et al., 2021), these studies are from strike-slip settings. Extending the geodetic observation of dip-slip earthquakes to the early 20th century, allows us to expand on the number of well-characterized normal earthquake ruptures, providing a rare insight into the nature of OFD within extensional fault systems.

2. Data and Methods

OIC has become a standard method for retrieving the surface displacement field created by large strike-slip earthquakes (e.g., Gold et al., 2021; Lauer et al., 2020; Leprince et al., 2007; Michel et al., 1999; Rosu et al., 2015; Van Puymbroeck et al., 2000; Zinke et al., 2019). To measure co-seismic displacements OIC compares the pixel shift between pre-earthquake and post-earthquake images (Leprince et al., 2007). The approach is optimally suited for the detection of horizontal ground motion, due to planar view of the pre- and post-earthquake images following orthorectification.

To retrieve 3-D surface displacements, we use an automatic workflow which utilizes structure-from-motion tools incorporated in the open-source Ames Stereo Pipeline (ASP) software (Beyer et al., 2018). We selected pre-event stereo-images acquired on 1st and 12th July 1947 and post-event photographs from 1st August 1977 that extend across a part of the rupture area (Figure 1). The images were acquired by U.S. Bureau of Reclamation and can be downloaded from the Earth Explorer website at no cost (<https://earthexplorer.usgs.gov/>). The scale of the images is 1:48,000 (ground footprint $\approx 11 \times 11$ km, resolution ≈ 1.1 m/px) for the pre-earthquake images and 1:28,000 (ground footprint $\approx 6 \times 6$ km, resolution ≈ 0.6 m/px) for the post-earthquake images; the resolution of the image scans is 1,000 dpi. Since the historical images suffer from film distortions, scanning artifacts, and image defects (Hollingsworth et al., 2012; Michel & Avouac, 2006), we built on the method described in Ajorlou et al. (2021) and Bhushan et al. (2021) and created high-resolution DEMs from the pre- and post-earthquake stereo-image pairs which were used to precisely orthorectify the pre- and post-earthquake aerial photographs at 1 m/px. Precise orthorectification is crucial to remove topographic distortion and to avoid the interference of residual stereoscopic signal with the tectonic displacement in the final correlation.

We use a semi-global matching (SGM) algorithm (Hirschmuller, 2007) implemented in ASP to correlate the images. As SGM is not optimized for sub-pixel performance (Ye et al., 2020), we employ a Bayesian Expectation Maximization (Bayes EM) sub-pixel refinement (Nefian et al., 2009), which reduces image noise, and gives a final precision of $\approx 1/10$ th pixel. The SGM correlation algorithm computes disparity values for every pixel in the image. However, the true spatial resolution of the final correlation is limited by the size of the sub-pixel refinement correlation kernel (21×21 pixels, minus the effects of a Gaussian windowing function). This means that despite the displacement being calculated for every pixel in the image (1 m/px), spatial variability is well-resolved at approximately 10 m length scales. The combination of the SGM and Bayes EM sub-pixel refinement produces correlation maps comparable to the displacement maps obtained from other correlation softwares a software optimized for motion tracking, such as COSI-Corr (Leprince et al., 2007) and MicMac (Rosu et al., 2015). The outcome of the correlation is a pair of high-resolution maps with E-W and N-S displacement.

The horizontal displacement maps only reveal a small proportion of the displacements associated with the extensional dip-slip faulting. To calculate the vertical offset we subtract the post-earthquake DEM from the pre-earthquake topography. Similar to previous studies (Barnhart et al., 2019; Delorme et al., 2020; Zhou et al., 2015), to minimize high frequency topographic artifacts associated with differencing of a laterally displaced surface, we shift the pre-earthquake DEM to the post-earthquake position (using the 2D horizontal displacement map) before differencing the heights. We employ quintic spline interpolation when shifting the pre-DEM, which helps to minimize resampling artifacts. To mitigate the impact of the correlated noise on the final results we use a random forest algorithm (Breiman, 2001) to learn the relationship between correlation bias, pre- and post-image reflectance and local topographic slope and aspect in non-deforming regions. The model is used to predict the

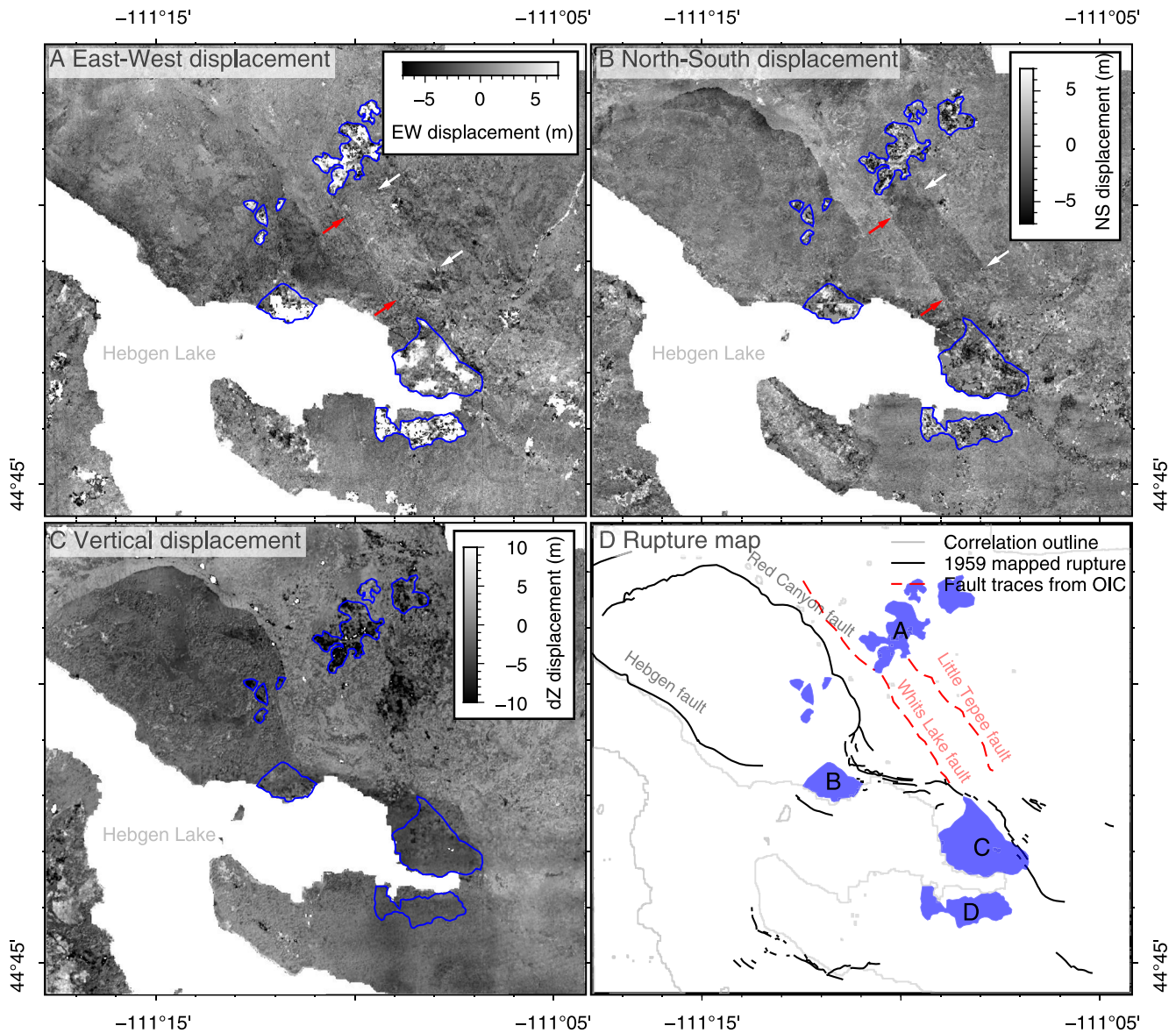


Figure 2. The correlation results show the (a) EW, (b) NS, (c) vertical displacement field from the image correlation of the pre- and post-earthquake aerial photographs and the DEM differencing (resolution: 10 m/pixel), and (d) rupture map highlighting the rupture traces mapped by USGS and detected from optical image correlation (OIC) results. Regions highlighted in blue indicate decorrelation caused by land-use change (d-panel (a)) or sediment deposition (d-panels (b–d)). N-S and E-W displacement components show the Whits Lake fault (red arrows) and the Little Tepee fault (white arrows) approximately 2 km east of the Red Canyon fault trace.

correlation bias, which is then removed (for the full details of the process and the discussion of the uncertainties see Text S1 in Supporting Information S1).

3. Results

Our Hebgen Lake correlations reveal the normal faults known to have ruptured in the mainshock, along with two newly discovered strike-slip faults located ~2 km east of the main surface rupture (Figure 2b). Of the four fault scarps mapped during the original field reconnaissance (Witkind et al., 1962), only the RCF has displacement values significantly above the noise threshold required for meaningful structural analysis. While the KF and the WFF are below the detection limit of OIC, the HF has proved challenging to characterize due to its proximity to the lake, which limits the extent over which pixels can be correlated in the hanging wall. Post-seismic deformation measured by geodetic leveling after the earthquake did not exceed 32 cm (Holdahl & Dzurisin, 1991).

Therefore, the deformation described in this study is largely co-seismic or related to aftershocks immediately following the earthquake. No large surface rupturing events are known from the post-earthquake period prior to acquisition of the post-event aerial images used in the analysis.

3.1. Characteristics of the Whits Lake Fault and the Little Tepee Fault

Our correlation results reveal two previously unrecognized strike-slip faults. These structures are clearly visible in the NS (Figure 2b), and to a lesser extent in the EW displacement maps (Figure 2a). They are located NE of the RCF and strike in a NW-SE direction. We refer to these faults as the Whits Lake fault (west) and the Little Tepee fault (east). The sense of motion on the Whits Lake fault is primarily right-lateral strike-slip with a minor compression; the mean fault-parallel, and vertical displacement values are 2.08 ± 0.1 and -0.36 ± 0.12 m, respectively. On the other hand, the Little Tepee fault is a left-lateral strike-slip with mean fault-parallel, and vertical component -1.9 ± 0.12 , and -0.6 ± 0.2 m, respectively. The fault-normal component on both faults is negligible. Likely, these faults were not identified in the initial field study because of the dense vegetation cover, the disconnected location relative to the RCF and HF, and the relatively small displacements (particularly in the vertical component).

3.2. On-Fault and Off-Fault Displacement Measurements

From the displacement maps, we extracted 105 stacked profiles along the RCF (stack dimensions 150×750 m). Fault-parallel, fault-perpendicular, and vertical offset was calculated for each profile (for the detailed calculations of the fault offset see Text S2 in Supporting Information S1). We did not collect any measurements from areas of visible distributed deformation (Figures 2a–2d & Figure 3b) to avoid inaccurate offset estimates due to noisy correlation results (the area coincides with the decorrelation region) and the absence of hanging wall data. The vertical slip profile along the Kirkwood Ridge section of the RCF has a characteristic arcuate shape with the highest displacement in the central part of the fault (Manighetti et al., 2001) (Figure 3a). The mean vertical displacement along the RCF is 3.2 ± 0.7 m, with minimum and maximum displacement values of -4.9 and 7.7 m, respectively. The horizontal component on the RCF is significantly smaller with mean fault-parallel offset 0.76 ± 0.6 m (min = -4.5 m, max = 6.8 m) and mean fault-perpendicular slip 2.4 ± 0.6 m (min = -3 m, max = 6.6 m) (Figure S3 in Supporting Information S1).

We compared the total dip-slip component determined in this study (calculated from the vertical and fault-perpendicular offset) to the existing field (Witkind, 1964) and LiDAR fault displacement measurements (Johnson et al., 2018) (Figure 3a). This comparison shows a systematic overestimate of the OIC results suggesting that a large proportion of the deformation was accommodated in the rock volume surrounding the fault as permanent damage. The residual offset was calculated from the difference between the field/LiDAR data and OIC measurements. The mean residual offset calculated from the OIC and field measurements is 1.5 m, with minimum -1.2 m and maximum 3.9 m. Subsequently, we used this data to calculate %OFD. Because OFD can be only positive, we exclude the negative residuals. The average %OFD from the OIC and field measurements is 42.1 ($1\sigma = 23.4\%$), with minimum 0.5% , maximum 100% , and median 45% . We use the same method to determine the offset residual from the OIC and LiDAR displacement estimates. The results of our calculations are mean = 1 m, minimum = -2.2 m, and maximum = 3.7 m. The mean percentage OFD calculated from OIC and LiDAR data is 59.7% ($1\sigma = 23.8\%$) with minimum, maximum, and median values of 0.5% , 92.2% , and 59.7% , respectively. In both cases, the highest offset residual and %OFD is recorded in the central part of the Kirkwood Ridge, approximately $3\text{--}4$ km from its northwest terminus (Figures 3b–3d).

4. Discussion

4.1. Kinematics of the Whits Lake Fault and the Little Tepee Fault

Extending the analysis beyond the known earthquake area reveals reactivated surface ruptures (Whits Lake fault and Little Tepee fault). The kinematics of these faults is dextral and sinistral strike-slip, which is inconsistent with the NE-SW extensional deformation style for the 1959 Hebgen Lake mainshock (Waite & Smith, 2004).

The right-lateral motion of the Whits Lake fault approximately coincides with the relocated focal mechanism for a $M6.1$ aftershock occurring at 08:41 (Doser, 1985). The original location of this event was ~ 20 km to the east

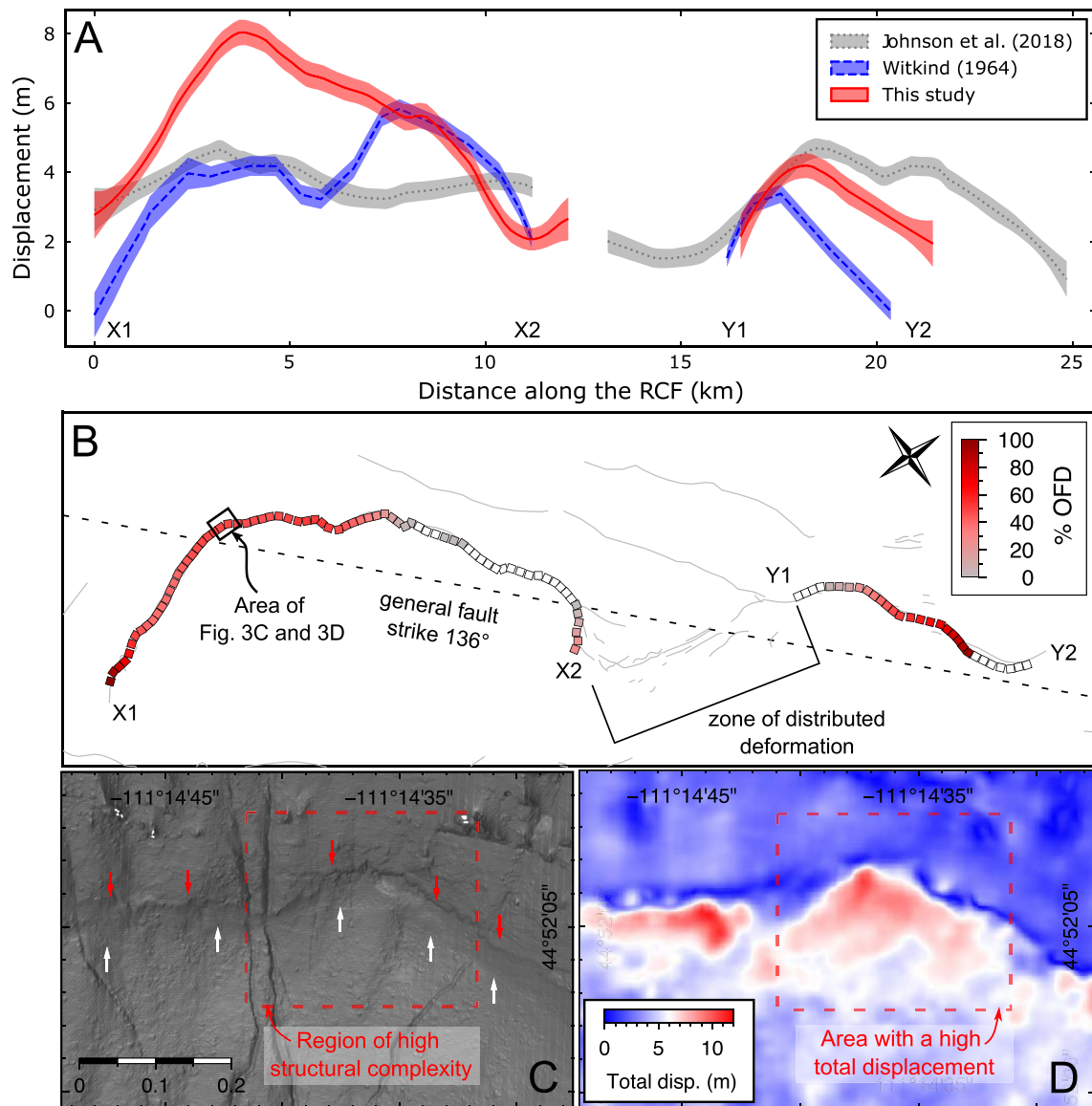


Figure 3. (a) LOESS regression for the LiDAR (Johnson et al., 2018), field (Witkind, 1964), and optical image correlation (OIC) data with envelopes showing the standard errors of the regression models. The OIC data represent the dip-slip component. (b) Color-coded percentages of off-fault deformation (OFD) shown in map view. White markers represent cases where %OFD is small or could not be determined due to negative residuals. (c) Lidar DEM with 0.5 m/pixel resolution adapted from Johnson et al. (2018), using terrain illumination conditions with altitude/azimuth = 10°/270°. The red and white arrows show the top and bottom of the fault scarp, respectively. The dashed rectangle highlights a zone of structural complexity (i.e., fault bend), which corresponds to the area of distributed deformation highlighted in panel (d).

(Doser, 1985), however, using multiple-events hypocentroidal decomposition relocation (previously described in, for example, McNamara et al. (2015); Nealy et al. (2017); Karasözen et al. (2019); and Pousse-Beltran et al. (2020) Text S3 in Supporting Information S1), we locate this aftershock ~6 km east of the Whits Lake fault. While the location uncertainty for this event is ~2 km (90% confidence), the results are still sensitive to details of which arrival times are used and how they are weighted. This means that relocated aftershocks could have an additional error of several km. Given these considerations, it is conceivable that the Whits Lake fault ruptured during the 08:41 aftershock. Nevertheless, due to the long time interval between the acquisition of the pre- and post-earthquake images, we cannot make this association with certainty. From the available focal mechanisms, the left-lateral motion of the Little Tepee fault appears to be consistent with the aftershock event that happened at 15:26 on 18 August 1959 (Doser, 1985) (Figure S6 in Supporting Information S1). However, the teleseismic earthquake relocations place this event ~30 km east of the surface rupture. Such a large distance does not fall

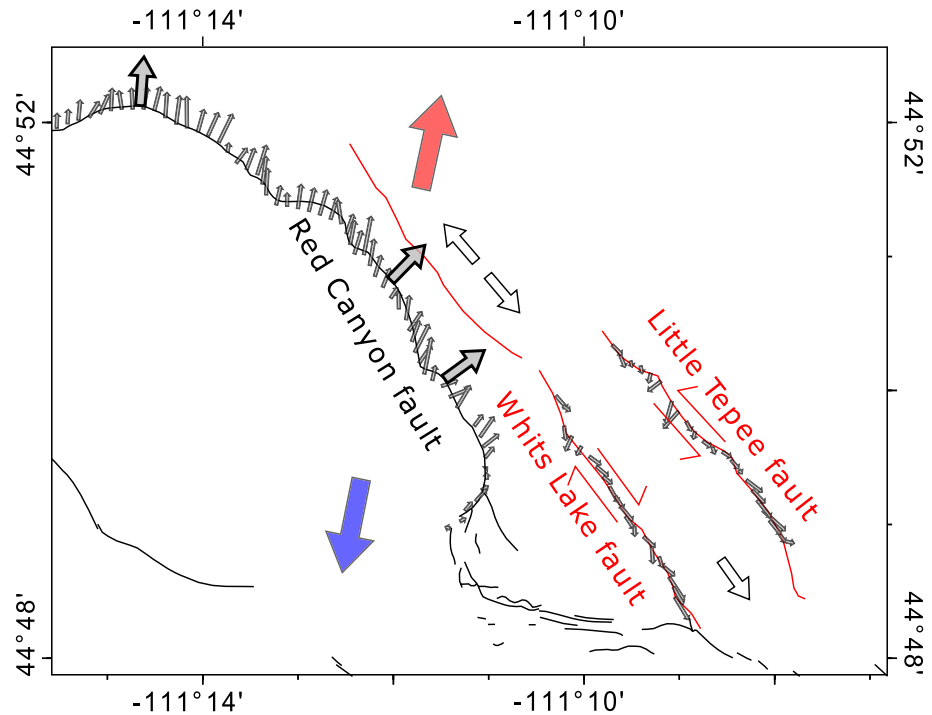


Figure 4. A map view of the Red Canyon fault (RCF), the Whits Lake fault and the Little Tepee fault (outlined in Figure 1). The large arrows show the movement of the blocks; small gray arrows show the displacement vector for each profile; large gray arrows show the average direction of the rotating vector field along the RCF. Large red and blue arrows are aligned in the direction of regional extension. Blue and red colors represent the subsidence and uplift caused by the 1959 event, respectively. White arrows show the possible direction of extension NE of the RCF and the SE-directed deformation within the microblock between the Whits Lake fault and the Little Tepee fault as determined from the OIC results.

within the confidence interval. Therefore, we cannot conclusively associate any obvious relocated aftershock with the Little Tepee rupture.

The strike-slip kinematics of the Whits Lake fault and Little Tepee fault favors the accommodation of strain induced by the mainshock rupture. The slip vector along the RCF rotates along-strike, remaining approximately perpendicular to the rupture trace. If the rupture propagated unilaterally from southeast to northwest (Doser, 1985), the changing slip vector would induce a zone of extension NE of the RCF (near 44.86°N 111.22°W) where the rupture bends from NS (north of Grayling) to EW (along Kirkwood Ridge). This zone of extension is oriented perpendicular to Kirkwood Ridge, and may itself be accommodated by the SE-directed expulsion of a micro-block between the Whits Lake and Little Tepee faults (Figure 4). Therefore, the kinematics of these two structures likely reflects internal block deformation, induced by the changing geometry of the mainshock rupture. The fault trace of the Whits Lake fault also coincides with a mapped geological thrust fault (Figure S7 in Supporting Information & S1). Hence, it is likely that this structure represents a zone of pre-existing weakness that was exploited to accommodate internal deformation around the mainshock rupture.

4.2. Qualitative and Quantitative Comparison of the OIC Data With the Pre-Existing Studies

We compare fault offsets estimated from optical correlation data with those measured in the field (Witkind, 1964), and inferred from post-event LiDAR data (Johnson et al., 2018). To make a meaningful comparison of our results with the values reported by Witkind (1964) and Johnson et al. (2018) we calculate the pure dip-slip component from the fault perpendicular and vertical offset measurements (the offset measurements collected in the field or by LiDAR do not account for horizontal movements). To reduce the influence of outliers, and make a more general comparison of the first order features in each data set, we approximate their trends using LOESS regression (Figure 3a). Comparison of the OIC data with the field measurements shows that, at some localities,

OIC-derived offsets are up to twice as large as field and LiDAR measurements (Figure 3b). Despite the systematically larger offset values obtained with OIC, the general trend of all datasets is comparable.

We attribute the larger offsets obtained with OIC to OFD distributed away from the fault plane. OFD represents distributed inelastic strain accommodated via secondary fracturing in the regions of increased structural complexity (e.g., fault bends) (Dolan & Haravitch, 2014; Gold et al., 2015) (Figure 3c). Factors such as rupture speed (Aben et al., 2020; Jara et al., 2021), and variable lithology (Zinke et al., 2014) also contribute to the off-fault component of slip, but to a lesser extent. Due to the distributed fracturing, the total displacement is accommodated across a wide fault zone, which extends across 47.2 m ($1\sigma = 18$ m), 56.2 m ($1\sigma = 19$ m), and 65.4 m ($1\sigma = 20$ m) for fault-parallel, fault-perpendicular, and vertical measurements, respectively. Considering the noise in the data, it is difficult to estimate the fault zone width with certainty. Nevertheless, our most robust measurements of fault zone width show little along-strike variation (Figure S5 in Supporting Information S1). Since the field measurements are usually collected across a very narrow aperture that does not extend beyond the immediate proximity of the fault scarp, they are not able to capture the total deformation accommodated across the wider fault zone. Similarly, Johnson et al. (2018) estimated fault offset from the relative height difference in the LiDAR between the footwall and the hanging wall topography. While this method can capture some OFD, it is possible that a large proportion of OFD remains unaccounted for, perhaps due to surface modification (e.g., erosion). In contrast, OIC is more sensitive to distributed deformation because it calculates offsets from the extrapolated trends of the footwall and hanging wall data at the location of the fault. Therefore, our OIC-derived fault offsets record the displacement accommodated across the fault zone, which comprises on-fault component and OFD extending up to a 100 m from the fault scarp.

To make a quantitative assessment, we compare the spatial distribution of the inelastic damage to the topographic slope, aspect, fault strike, and geological strike (Figure S4 in Supporting Information S1). For a robust comparison, we used the data from the NW section of the RCF where the fault scarp is very clear in the displacement field, and we can make high-confidence offset measurements. The first order observations indicate that the complex geometry and geological setting may prevent the localization of the earthquake-related surface deformation. This is expressed as a zone of distributed deformation north of Grayling. However, we did not include these data in the quantitative analysis due to the absence of a clear fault scarp, low confidence displacement measurements, and the absence of hanging wall data. The quantitative assessment shows a similar trend to the OFD estimates from the data collected along the ridge section of the RCF; the displacement is less localized in the areas where the local strike of the fault deviates from the general strike determined from seismological data (Figure 3b). Apart from the structural complexity, the deformation surrounding the RCF could also be impacted by gravitational processes associated with the steep topography, as well as down-dip variations in fault geometry. Indeed, we see some local excess of slip on the fault plane, compared to the surrounding off-fault region, as was documented in the 2016 Norcia earthquake (Delorme et al., 2020), where this difference was attributed to local gravity-driven processes.

The substantially larger coseismic displacements retrieved by OIC at the surface may contribute to resolving the disparity between the seismologically derived moment, and the moment inferred from extrapolating surface offsets at depth. Field measurements yield moments that are 50% lower than seismological estimates (Doser, 1985). However, if the field measurements are underestimated by up to 50%, as indicated by our data, the two moment estimates are comparable. Nevertheless, joint inversion of available geodetic data to obtain the fault slip distribution would be needed to better resolve the down-dip variability in fault slip, and better quantify the extent of SSD for the Hebgen Lake earthquake. Such an endeavor would need to take account of the complicated fault geometry, especially at depth, which will likely have a strong impact on the inversion.

5. Conclusions

In this work, we extend the application of OIC to the study of historical dip-slip earthquakes, widening the window of geodetic observation to >60 years. Using a combination of OIC and DEM differencing we resolve the 3-D displacement field produced by the 1959 Hebgen Lake earthquake. We also identify previously unrecognized ruptures on the Whits Lake fault and the Little Tepee fault, which may reflect internal deformation of the surrounding region during the early postseismic period. OIC offset estimates for the RCF are higher than the offsets measured in the field (Witkind, 1964), or inferred from post-earthquake LiDAR data (Johnson

et al., 2018). We attribute this discrepancy to off-fault damage, which is not well-resolved in the field or LiDAR estimates. The spatial distribution of OFD may correlate (weakly) with fault strike and geometric variability. Failure to account for off-fault damage can underestimate the total fault offset and lead to incorrect estimates of the magnitude and seismic moment from geologic data. Nevertheless, it remains unclear if the Hebgen Lake earthquake featured substantial SSD, pending a future fault slip inversion study integrating all available geodetic data.

Data Availability Statement

This work uses high resolution historical aerial images available at <https://earthexplorer.usgs.gov/>. The processing workflow was designed in Ames Stereo Pipeline (<https://stereopipeline.readthedocs.io/en/latest/index.html>) (Beyer et al., 2018). We used COSI-Corr (Leprince et al., 2007) and MATLAB, for the post-processing and data analysis, respectively. The topographic map in Figure 1 is ESRI Shaded Relief available at ArcGIS repository https://server.arcgisonline.com/arcgis/rest/services/World_Shaded_Relief/MapServer via QGIS. The initial locations of the mainshock and aftershocks are from the USGS earthquake catalog <https://earthquake.usgs.gov/earthquakes/search/>. The 3-D displacement maps are available at <https://doi.org/10.5281/zenodo.6803257>, 3-D displacement profiles from Red Canyon fault used for the analysis can be found at <https://doi.org/10.5281/zenodo.6921825>, the displacement profiles collected along the Grayling Arm can be found at <https://doi.org/10.5281/zenodo.6921937>.

Acknowledgments

L. Andreuttiova was supported by the Natural Environment Research Council Doctoral Training Partnership (Grant No. NE/L002485/1). J. Hollingsworth was supported by grants from BQR, Labex, and CNES. We thank Sophie Giffard-Roisin and Michel Bouchon for helpful discussion. We would also like to thank two anonymous reviewers who contributed to the quality and clarity of this article.

References

- Aben, F. M., Brantut, N., & Mitchell, T. M. (2020). Off-fault damage characterization during and after experimental quasi-static and dynamic rupture in crustal rock from laboratory P wave tomography and microstructures. *Journal of Geophysical Research: Solid Earth*, 125(8), e2020JB019860. <https://doi.org/10.1029/2020jb019860>
- Ajorlou, N., Hollingsworth, J., Mousavi, Z., Ghods, A., & Masoumi, Z. (2021). Characterizing near-field surface deformation in the 1990 Rudbar earthquake (Iran) using optical image correlation. *Geochemistry, Geophysics, Geosystems*, 22(6), e2021GC009704. <https://doi.org/10.1029/2021gc009704>
- Barnhart, W. D., Gold, R. D., Shea, H. N., Peterson, K. E., Briggs, R. W., & Harbor, D. J. (2019). Vertical coseismic offsets derived from high-resolution stereogrammetric DSM differencing: The 2013 Baluchistan, Pakistan earthquake. *Journal of Geophysical Research: Solid Earth*, 124(6), 6039–6055. <https://doi.org/10.1029/2018jb017107>
- Barrientos, S., Stein, R., & Ward, S. (1989). Comparison of the Hebgen Lake, Montana, and the 1983 Borah Peak, Idaho, earthquakes from geodetic observations. *Bulletin of the Seismological Society of America*, 79(6), 2018. <https://doi.org/10.1785/bssa0790062018a>
- Beyer, R. A., Alexandrov, O., & McMichael, S. (2018). The Ames Stereo Pipeline: NASA's open source software for deriving and processing terrain data. *Earth and Space Science*, 5(9), 537–548. <https://doi.org/10.1029/2018ea000409>
- Bhushan, S., Shean, D., Alexandrov, O., & Henderson, S. (2021). Automated digital elevation model (DEM) generation from very-high-resolution Planet SkySat triplet stereo and video imagery. *ISPRS Journal of Photogrammetry and Remote Sensing*, 173, 151–165. <https://doi.org/10.1016/j.isprsjprs.2020.12.012>
- Breiman, L. (2001). Random forests. *Machine Learning*, 45(1), 5–32. <https://doi.org/10.1023/a:1010933404324>
- Chang, W.-L., Smith, R. B., & Puskas, C. M. (2013). Effects of lithospheric viscoelastic relaxation on the contemporary deformation following the 1959 Mw 7.3 Hebgen Lake, Montana, earthquake and other areas of the intermountain seismic belt. *Geochemistry, Geophysics, Geosystems*, 14(1), 1–17. <https://doi.org/10.1029/2012gc004424>
- Delorme, A., Grandin, R., Klinger, Y., Pierrot-Deseilligny, M., Feuillet, N., Jacques, E., et al. (2020). Complex deformation at shallow depth during the 30 October 2016 Mw 6.5 Norcia earthquake: Interference between tectonic and gravity processes? *Tectonics*, 39(2), e2019TC005596. <https://doi.org/10.1029/2019tc005596>
- Dolan, J. F., & Haravitch, B. D. (2014). How well do surface slip measurements track slip at depth in large strike-slip earthquakes? The importance of fault structural maturity in controlling on-fault slip versus off-fault surface deformation. *Earth and Planetary Science Letters*, 388, 38–47. <https://doi.org/10.1016/j.epsl.2013.11.043>
- Dominguez, S., Avouac, J.-P., & Michel, R. (2003). Horizontal coseismic deformation of the 1999 Chi-Chi earthquake measured from SPOT satellite images: Implications for the seismic cycle along the western foothills of central Taiwan. *Journal of Geophysical Research: Solid Earth*, 108(B2). Portico. <https://doi.org/10.1029/2001jb000951>
- Doser, D. I. (1985). Source parameters and faulting processes of the 1959 Hebgen Lake, Montana, earthquake sequence. *Journal of Geophysical Research*, 90(B6), 4537–4555. <https://doi.org/10.1029/jb090ib06p04537>
- Fialko, Y., Sandwell, D., Simons, M., & Rosen, P. (2005). Three-dimensional deformation caused by the Bam, Iran, earthquake and the origin of shallow slip deficit. *Nature*, 435(7040), 295–299. <https://doi.org/10.1038/nature03425>
- Gold, R. D., DuRoss, C. B., & Barnhart, W. D. (2021). Coseismic surface displacement in the 2019 Ridgecrest earthquakes: Comparison of field measurements and optical image correlation results. *Geochemistry, Geophysics, Geosystems*, 22(3), e2020GC009326. <https://doi.org/10.1029/2020gc009326>
- Gold, R. D., Reitman, N. G., Briggs, R. W., Barnhart, W. D., Hayes, G. P., & Wilson, E. (2015). On-and off-fault deformation associated with the September 2013 Mw 7.7 Baluchistan earthquake: Implications for geologic slip rate measurements. *Tectonophysics*, 660, 65–78. <https://doi.org/10.1016/j.tecto.2015.08.019>
- Heaton, T. H. (1982). The 1971 San Fernando earthquake: A double event?. *Bulletin of the Seismological Society of America*, 72(6A), 2037–2062. <https://doi.org/10.1785/bssa07206a2037>
- Hirschmuller, H. (2007). Stereo processing by semiglobal matching and mutual information. *IEEE Transactions on Pattern Analysis and Machine Intelligence*, 30(2), 328–341. <https://doi.org/10.1109/tpami.2007.1166>

- Holdahl, S. R., & Dzurisin, D. (1991). Time-dependent models of vertical deformation for the Yellowstone-Hebgen Lake Region, 1923–1987. *Journal of Geophysical Research*, *96*(B2), 2465–2483. <https://doi.org/10.1029/90jb02011>
- Hollingsworth, J., Leprince, S., Ayoub, F., & Avouac, J.-P. (2012). Deformation during the 1975–1984 Krafla rifting crisis, NE Iceland, measured from historical optical imagery. *Journal of Geophysical Research*, *117*(B11), B11407. <https://doi.org/10.1029/2012jb009140>
- Jara, J., Bruhat, L., Thomas, M. Y., Antoine, S. L., Okubo, K., Rougier, E., et al. (2021). Signature of transition to supershear rupture speed in the coseismic off-fault damage zone. *Proceedings of the Royal Society A*, *477*(2255), 20210364. <https://doi.org/10.1098/rspa.2021.0364>
- Jin, Z., & Fialko, Y. (2021). Coseismic and early postseismic deformation due to the 2021 M_{7.4} Maduo (China) earthquake. *Geophysical Research Letters*, *48*(21), e2021GL095213. <https://doi.org/10.1029/2021gl095213>
- Johnson, K. L., Nissen, E., & Lajoie, L. (2018). Surface rupture morphology and vertical slip distribution of the 1959 M_w 7.2 Hebgen Lake (Montana) earthquake from airborne lidar topography. *Journal of Geophysical Research: Solid Earth*, *123*(9), 8229–8248. <https://doi.org/10.1029/2017jb015039>
- Karasözen, E., Nissen, E., Bergman, E. A., & Ghods, A. (2019). Seismotectonics of the Zagros (Iran) from orogen-wide, calibrated earthquake relocations. *Journal of Geophysical Research: Solid Earth*, *124*(8), 9109–9129. <https://doi.org/10.1029/2019jb017336>
- Lauer, B., Grandin, R., & Klinger, Y. (2020). Fault geometry and slip distribution of the 2013 M_w 7.7 Balochistan earthquake from inversions of SAR and optical data. *Journal of Geophysical Research: Solid Earth*, *125*(7), e2019JB018380. <https://doi.org/10.1029/2019jb018380>
- Leprince, S., Barbot, S., Ayoub, F., & Avouac, J.-P. (2007). Automatic and precise orthorectification, coregistration, and subpixel correlation of satellite images, application to ground deformation measurements. *IEEE Transactions on Geoscience and Remote Sensing*, *45*(6), 1529–1558. <https://doi.org/10.1109/tgrs.2006.888937>
- Magen, Y., Ziv, A., Inbal, A., Baer, G., & Hollingsworth, J. (2020). Fault rerupture during the July 2019 Ridgecrest earthquake pair from joint slip inversion of InSAR, optical imagery, and GPS. *Bulletin of the Seismological Society of America*, *110*(4), 1627–1643. <https://doi.org/10.1785/0120200024>
- Manighetti, I., King, G., Gaudemer, Y., Scholz, C., & Doubre, C. (2001). Slip accumulation and lateral propagation of active normal faults in Afar. *Journal of Geophysical Research*, *106*(B7), 13667–13696. <https://doi.org/10.1029/2000jb900471>
- Marchandon, M., Hollingsworth, J., & Radiguet, M. (2021). Origin of the shallow slip deficit on a strike slip fault: Influence of elastic structure, topography, data coverage, and noise. *Earth and Planetary Science Letters*, *554*, 116696. <https://doi.org/10.1016/j.epsl.2020.116696>
- McNamara, D. E., Benz, H. M., Herrmann, R. B., Bergman, E. A., Earle, P., Holland, A., et al. (2015). Earthquake hypocenters and focal mechanisms in central Oklahoma reveal a complex system of reactivated subsurface strike-slip faulting. *Geophysical Research Letters*, *42*(8), 2742–2749. <https://doi.org/10.1002/2014gl062730>
- Michel, R., & Avouac, J.-P. (2006). Coseismic surface deformation from air photos: The Kickapoo step over in the 1992 Landers rupture. *Journal of Geophysical Research*, *111*(B3), B03408. <https://doi.org/10.1029/2005jb003776>
- Michel, R., Avouac, J.-P., & Taboury, J. (1999). Measuring ground displacements from SAR amplitude images: Application to the Landers earthquake. *Geophysical Research Letters*, *26*(7), 875–878. <https://doi.org/10.1029/1999gl900138>
- Milliner, C., Donnellan, A., Aati, S., Avouac, J.-P., Zinke, R., Dolan, J. F., et al. (2021). Bookshelf kinematics and the effect of dilatation on fault zone inelastic deformation: Examples from optical image correlation measurements of the 2019 Ridgecrest earthquake sequence. *Journal of Geophysical Research: Solid Earth*, *126*(3), e2020JB020551. <https://doi.org/10.1029/2020jb020551>
- Milliner, C. W., Dolan, J. F., Hollingsworth, J., Leprince, S., Ayoub, F., & Sammis, C. G. (2015). Quantifying near-field and off-fault deformation patterns of the 1992 M_w 7.3 Landers earthquake. *Geochemistry, Geophysics, Geosystems*, *16*(5), 1577–1598. <https://doi.org/10.1002/2014gc005693>
- Mitchell, T., & Faulkner, D. (2009). The nature and origin of off-fault damage surrounding strike-slip fault zones with a wide range of displacements: A field study from the Atacama fault system, northern Chile. *Journal of Structural Geology*, *31*(8), 802–816. <https://doi.org/10.1016/j.jsg.2009.05.002>
- Myers, W. B., & Hamilton, W. (1964). Deformation accompanying the Hebgen Lake earthquake of August 17, 1959.
- Nealy, J. L., Benz, H. M., Hayes, G. P., Bergman, E. A., & Barnhart, W. D. (2017). The 2008 Wells, Nevada, earthquake sequence: Source constraints using calibrated multiple-event relocation and InSAR. *Bulletin of the Seismological Society of America*, *107*(3), 1107–1117. <https://doi.org/10.1785/0120160298>
- Neely, J. S., & Stein, S. (2021). Why do continental normal fault earthquakes have smaller maximum magnitudes? *Tectonophysics*, *809*, 228854. <https://doi.org/10.1016/j.tecto.2021.228854>
- Nefian, A. V., Husmann, K., Broxton, M., To, V., Lundy, M., & Hancher, M. D. (2009). A Bayesian formulation for sub-pixel refinement in stereo orbital imagery. In *2009 16th IEEE international conference on image processing (ICIP)* (pp. 2361–2364). IEEE.
- Oglesby, D. D., Archuleta, R. J., & Nielsen, S. B. (2000). The three-dimensional dynamics of dipping faults. *Bulletin of the Seismological Society of America*, *90*(3), 616–628. <https://doi.org/10.1785/0119990113>
- Ostermeijer, G. A., Mitchell, T. M., Aben, F. M., Dorsey, M. T., Browning, J., Rockwell, T. K., et al. (2020). Damage zone heterogeneity on seismogenic faults in crystalline rock: a field study of the Borrego Fault, Baja California. *Journal of Structural Geology*, *137*, 104016. <https://doi.org/10.1016/j.jsg.2020.104016>
- Pousse-Beltran, L., Nissen, E., Bergman, E. A., Cambaz, M. D., Gaudreau, É., Karasözen, E., & Tan, F. (2020). The 2020 M_w 6.8 Elazığ (Turkey) earthquake reveals rupture behavior of the East Anatolian Fault. *Geophysical Research Letters*, *47*(13), e2020GL088136. <https://doi.org/10.1029/2020gl088136>
- Rosu, A.-M., Pierrot-Deseilligny, M., Delorme, A., Binet, R., & Klinger, Y. (2015). Measurement of ground displacement from optical satellite image correlation using the free open-source software MicMac. *ISPRS Journal of Photogrammetry and Remote Sensing*, *100*, 48–59. <https://doi.org/10.1016/j.isprsjprs.2014.03.002>
- Ryall, A. (1962). The Hebgen Lake, Montana, earthquake of August 18, 1959: P waves. *Bulletin of the Seismological Society of America*, *52*(2), 235–271. <https://doi.org/10.1785/bssa0520020235>
- Schwartz, D., Hecker, S., Stenner, H., Haller, K. M., Pierce, K. L., Lageson, D. R., & Machette, M. (2009). The 1959 Hebgen Lake, Montana, surface rupture and record of late-Pleistocene-Holocene earthquakes. In *Bulletin biological society of America annual meeting*, (Vol. 41, p. 53).
- Scott, C. P., Arrowsmith, J. R., Nissen, E., Lajoie, L., Maruyama, T., & Chiba, T. (2018). The M7 2016 Kumamoto, Japan, earthquake: 3-d deformation along the fault and within the damage zone constrained from differential lidar topography. *Journal of Geophysical Research: Solid Earth*, *123*(7), 6138–6155. <https://doi.org/10.1029/2018jb015581>
- Smith, R. B., & Sbar, M. L. (1974). Contemporary tectonics and seismicity of the western United States with emphasis on the Intermountain Seismic Belt. *The Geological Society of America Bulletin*, *85*(8), 1205–1218. [https://doi.org/10.1130/0016-7606\(1974\)85<1205:ctasot>2.0.co;2](https://doi.org/10.1130/0016-7606(1974)85<1205:ctasot>2.0.co;2)
- Van Puymbroeck, N., Michel, R., Binet, R., Avouac, J.-P., & Taboury, J. (2000). Measuring earthquakes from optical satellite images. *Applied Optics*, *39*(20), 3486–3494. <https://doi.org/10.1364/ao.39.003486>

- Waite, G. P., & Smith, R. B. (2004). Seismotectonics and stress field of the Yellowstone volcanic plateau from earthquake first-motions and other indicators. *Journal of Geophysical Research*, *109*(B2), B02301. <https://doi.org/10.1029/2003jb002675>
- Witkind, I. J. (1964). *Reactivated faults north of Hebgen Lake*. US Government Printing Office.
- Witkind, I. J., Myers, W. B., Hadley, J. B., Hamilton, W., & Fraser, G. D. (1962). Geologic features of the earthquake at Hebgen Lake, Montana, August 17, 1959. *Bulletin of the Seismological Society of America*, *52*(2), 163–180. <https://doi.org/10.1785/bssa0520020163>
- Xu, G., Xu, C., Wen, Y., & Yin, Z. (2019). Coseismic and postseismic deformation of the 2016 M_w 6.2 Lampa earthquake, southern Peru, constrained by interferometric synthetic aperture radar. *Journal of Geophysical Research: Solid Earth*, *124*(4), 4250–4272. <https://doi.org/10.1029/2018jb016572>
- Xu, X., Sandwell, D. T., Ward, L. A., Milliner, C. W., Smith-Konter, B. R., Fang, P., & Bock, Y. (2020). Surface deformation associated with fractures near the 2019 Ridgecrest earthquake sequence. *Science*, *370*(6516), 605–608. <https://doi.org/10.1126/science.abd1690>
- Xu, X., Tong, X., Sandwell, D. T., Milliner, C. W., Dolan, J. F., Hollingsworth, J., et al. (2016). Refining the shallow slip deficit. *Geophysical Journal International*, *204*(3), 1867–1886. <https://doi.org/10.1093/gji/ggv563>
- Ye, Z., Xu, Y., Chen, H., Zhu, J., Tong, X., & Stilla, U. (2020). Area-based dense image matching with subpixel accuracy for remote sensing applications: Practical analysis and comparative study. *Remote Sensing*, *12*(4), 696. <https://doi.org/10.3390/rs12040696>
- Zhou, Y., Parsons, B., Elliott, J. R., Barisin, I., & Walker, R. T. (2015). Assessing the ability of Pleiades stereo imagery to determine height changes in earthquakes: A case study for the El Mayor-Cucapah epicentral area. *Journal of Geophysical Research: Solid Earth*, *120*(12), 8793–8808. <https://doi.org/10.1002/2015jb012358>
- Zinke, R., Hollingsworth, J., & Dolan, J. F. (2014). Surface slip and off-fault deformation patterns in the 2013 M_w 7.7 Balochistan, Pakistan earthquake: Implications for controls on the distribution of near-surface coseismic slip. *Geochemistry, Geophysics, Geosystems*, *15*(12), 5034–5050. <https://doi.org/10.1002/2014gc005538>
- Zinke, R., Hollingsworth, J., Dolan, J. F., & Van Dissen, R. (2019). Three-dimensional surface deformation in the 2016 M_w 7.8 Kaikōura, New Zealand, earthquake from optical image correlation: Implications for strain localization and long-term evolution of the Pacific-Australian plate boundary. *Geochemistry, Geophysics, Geosystems*, *20*(3), 1609–1628. <https://doi.org/10.1029/2018gc007951>
- Zreda, M., & Noller, J. S. (1998). Ages of prehistoric earthquakes revealed by cosmogenic chlorine-36 in a bedrock fault scarp at Hebgen Lake. *Science*, *282*(5391), 1097–1099. <https://doi.org/10.1126/science.282.5391.1097>